THE JOURNAL OF PHYSICAL CHEMISTRY A

 VOLUME 109, NUMBER 5, FEBRUARY 10, 2005

ARTICLES

Doubly Vibrationally Enhanced Four-Wave Mixing in Crotononitrile

Nicholas J. Condon† and John C. Wright*

Department of Chemistry, 1101 University Avenue, University of Wisconsin, Madison, Wisconsin 53706

Received: September 7, 2004; In Final Form: November 17, 2004

Doubly vibrationally enhanced (DOVE) resonances have been observed in the infrared four-wave mixing (IRFWM) spectra of crotononitrile. The 2D DOVE-FWM spectra of the cis and trans isomers of crotononitrile showed cross peaks between the C≡N stretching fundamental and the C≡N + C═C stretch and the C≡N + C−C stretch combination bands for each of the two isomers that were observed, demonstrating the isomer selectivity of DOVE-IRFWM. Frequency-domain simulations were able to reproduce the features of the observed spectra, so the values for the nonlinearity and dephasing rates of all of the nonlinear processes could be measured. The results are compared to the calculations of the third-order susceptibility based on the transition moments, line positions, and line widths observed in the infrared absorption and the Raman spectra of crotononitrile.

Introduction

Coherent multidimensional vibrational spectroscopy (CMDVS) promises to create new chemical measurement tools for investigating complex samples.[1,2] Multidimensional spectroscopy provides selective enhancements of the spectral features associated with inter- and intramolecular interactions including resolution enhancements for reducing spectral broadening, component selectivity for isolating individual components in complex mixtures, correlation information about relationships between different spectral features, and time resolution to provide structural information on ultrafast time scales. The capability of 2D vibrational spectroscopy has been demonstrated by doubly vibrationally enhanced (DOVE) and triply vibrationally enhanced (TRIVE) four-wave mixing (FWM),[3−6] heterodyne-detected stimulated photon-echo spectroscopy,[7−9] and pump−probe spectroscopy.[10−12] Cross peaks appear in the 2D spectra between modes that are coupled by intra- and intermolecular interactions. In DOVE methods, the cross-peak intensity depends on the coupling-induced combination-band transitions in one or more of the FWM resonances. In TRIVE and stimulated photon-echo methods, the cross-peak intensity depends on the incomplete destructive interference between coherence pathways that is caused by coupling-induced anharmonicities that remove the pathways' equivalence. Coupling can occur from through-space transition-dipole coupling or through-bond coupling in both cases.

In this paper, we use crotononitrile (C_4H_5N, 2-butenenitrile) as a model system for exploring the coupling between different modes in a simple conjugated π-bonded system. The coherent 2D spectra are dominated by three coherence pathways that quantum mechanically interfere at the amplitude level to change the line shapes, line intensities, and line widths. We use simulations of the 2D spectra to find the third-order susceptibility of all of the important pathways, and we estimate the dephasing rates of the different DOVE coherences including the double vibrational quantum coherences that define the multidimensional capabilities of the method. We compare the results to the simpler and previously studied acetonitrile system.[4,13] Finally, we demonstrate that DOVE-FWM can

* Corresponding author. E-mail: wright@chem.wisc.edu.
† Current address: Naval Research Laboratories, Washington, D.C. 20375-5338.

10.1021/jp045963p CCC: $30.25
Published on Web 01/11/2005

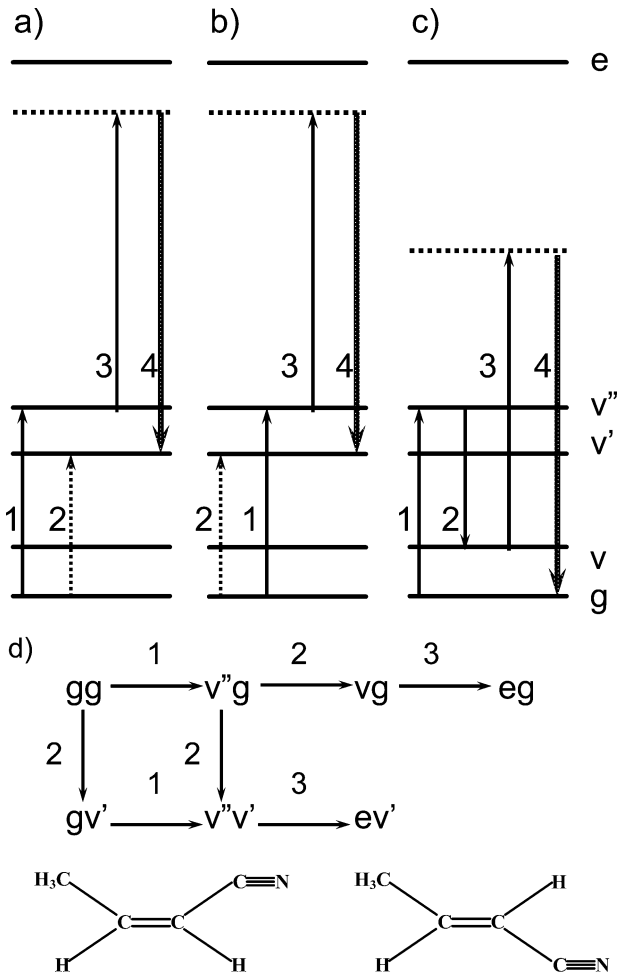

Figure 1. Resonances in the (a) DOVE-IRα, (b) DOVE-IRβ, and (c) DOVE-Raman pathways. The flow of coherences following each interaction with the electromagnetic field are shown in d, whereas the cis and trans forms of crotonitrile are shown on the bottom.

resolve the contributions of the crotononitrile cis and trans isomers.

Theory

DOVE-FWM requires the focusing of three coherent beams with frequencies ω_1, ω_2, and ω_3 into a sample and the monitoring of the intensity of the output beam created at $\omega_4 = \omega_1 - \omega_2 + \omega_3$ as a function of ω_1 and ω_2. The ω_1 and ω_2 frequencies induce two infrared vibrational transitions involving separate modes, and the ω_3 and ω_4 beams induce a Raman transition between the two coupled modes. The three excitation beams create a series of new coherences, $\rho_{ij} \equiv c_i^* c_j$,where c_i is the time-dependent wave function's amplitude for state i. In bra-ket notation, the coherence is $|i\rangle\langle j|$. Parts a−c of Figure 1 show the WMEL diagrams for the DOVE-IRα, DOVE-IRβ, and DOVE-Raman resonances, respectively.[14] The arrows indicate transitions between states, either on the ket (solid arrows) or bra (dotted arrows) side of the coherence, and the numbers label the frequency of the excitation lasers. The υ, υ', and υ'' label the vibrational states where υ and υ' represent two different vibrational modes and υ'' is the combination band of υ and υ'. The dotted virtual level arises from the excited electronic states represented by state e. Figure 1d shows the interconnections of the coherence pathways that involve the two vibrational resonances of the DOVE processes. Neglecting the singly vibrationally enhanced (SIVE) pathways that involve one vibrational resonance, we can write the hyperpolarizability, γ_i, for component i as

$$\gamma_i = A + \frac{B}{(\omega_{\upsilon g} - \omega_1 + \omega_2 - i\Gamma_{\upsilon g})} + C\left(-\frac{1}{(\omega_{\upsilon'' g} - \omega_1 - i\Gamma_{\upsilon'' g})(\omega_{\upsilon'' \upsilon'} - \omega_1 + \omega_2 - i\Gamma_{\upsilon'' \upsilon'})} + \frac{1}{(\omega_{\upsilon' g} - \omega_2 + i\Gamma_{\upsilon' g})(\omega_{\upsilon'' \upsilon'} - \omega_1 + \omega_2 - i\Gamma_{\upsilon'' \upsilon'})} + \frac{1}{(\omega_{\upsilon'' g} - \omega_1 - i\Gamma_{\upsilon'' g})(\omega_{\upsilon g} - \omega_1 + \omega_2 - i\Gamma_{\upsilon g})}\right) \quad (1)$$

where ω_{mn} and Γ_{mn} are the frequency differences and dephasing rates for states m and n and A, B, and C are fitting constants that include the dipole moments and nonresonant detuning factors involving nonresonant electronic states.[1] The five terms correspond to the nonresonant background, coherent anti-Stokes Raman scattering (CARS), the DOVE-IRα and -β pathways, and the DOVE-Raman pathway, respectively. Although the hyperpolarizability is written as a scalar quantity and refers to only one set of polarization directions relative to an oriented molecule, it is actually a fourth-rank tensor that defines the response to any set of polarization conditions.

Because the experiment measures the effects of many molecules, it is necessary to find the ensemble average of the hyperpolarizability over all of the molecular orientations and energy states represented by any inhomogeneous broadening. Because we do not see any effects of inhomogeneous broadening in our experiments, we assume that all of the molecules have identical energy states. We also assume (for simplicity) that the tensor components of the hyperpolarizability, γ, are directly proportional to those of the third-order susceptibility, $\chi^{(3)}$. Under these conditions, the $\chi^{(3)}_{1111}$ that is appropriate for the parallel polarization conditions of our experiment becomes

$$\chi_i = N_i F \gamma_i \quad (2)$$

where N_i is the component's concentration, F is the field enhancement factor for the solution where $F = F_1F_2F_3$, $F_a = (n_a^2 + 2)/3$, and n_a is the refractive index at the excitation frequency, ω_a. The FWM intensity, I_4, for a sample in a windowed sample cell is

$$I_4 \propto |\sum_i M_s \chi_i^{(3)} + M_w \chi_w^{(3)}|^2 I_1 I_2 I_3 \quad (3)$$

where M_s and M_w are the correction factors for phase matching and frequency-dependent changes in the absorption and refractive index of either the sample or the windows, respectively.[15−17] Scans are always performed by fixing the frequency of ω_1 or ω_2 and scanning the other frequency. The scanned frequency is chosen so the changes in the M factors in eq 3 remain as small as possible during the scan. To eliminate the intensity drift from experiments done over a long time period, we normalized the individual spectra to a spectral feature that does not exhibit additional resonances during any scan.

Equation 3 shows that the intensity involves cross terms between different nonlinear processes and components. These cross terms represent amplitude-level interferences that change the line shapes and intensities of resonances. The relative contributions from all of the nonlinear processes and components depend on the concentrations, amplitudes, detuning factors, and dephasing rates shown in eq 1. This situation is different from 1D incoherent spectroscopies where the dephasing rate is

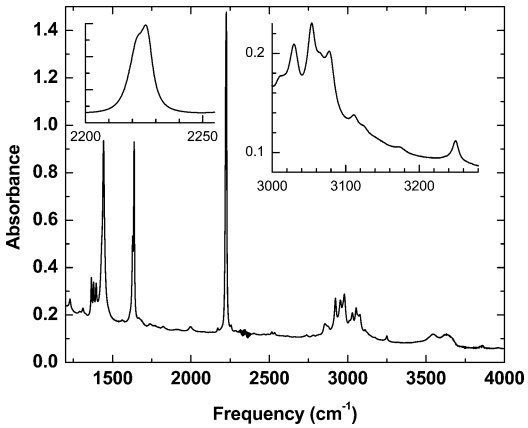

Figure 2. Infrared spectrum of crotononitrile.

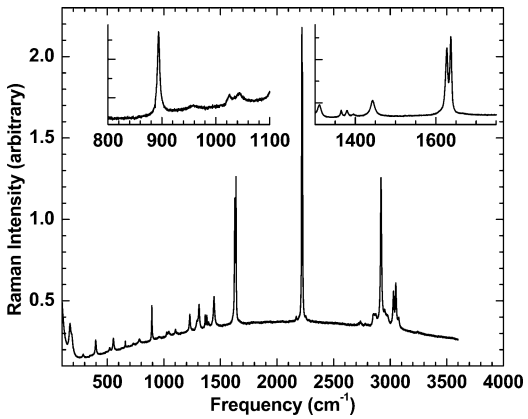

Figure 3. Raman spectrum of crotononitrile.

established from the line width of the homogeneous part of the line shape. The detailed fitting of the line shapes and intensities allows one to determine all of the contributions to the FWM.[13,18,19] By including a component in the sample mixture with a known $\chi^{(3)}$ for a particular coherence pathway, we can determine the values for $\chi^{(3)}$ and the coherence dephasing rates of all of the pathways and components.

Experimental Section

The details of the experimental system have been previously published.[4,20,21] Briefly, two optical parametric oscillator/amplifiers were excited by a seeded, 3-ns Nd:YAG laser to create two infrared beams that are independently tunable from 1.45 to 4.6 μm. The two infrared beams (frequencies of ω_1 and ω_2) were focused into the sample with the 14.2° angle required for phase matching. A portion of the frequency-doubled Nd:YAG beam (frequency ω_3) was aligned with the ω_1 beam and was also focused into the sample. All of the excitation beams were identically polarized. The output beam created at $\omega_4 = \omega_1 - \omega_2 + \omega_3$ was isolated with an aperture, directed into a double monochromator, and detected with a photomultiplier. No polarization selection was used. The monochromator band pass was set to discriminate between ω_3 and ω_4 but did not provide any spectral resolution of the output frequency.

The sample was a commercially available crotononitrile mixture (ca. 50:50) of the cis and trans isomers shown on the bottom of Figure 1. The infrared, Raman, and near-infrared spectra of this mixture are shown in Figures 2−4. Table 1 summarizes the frequencies and line widths of the relevant peaks along with their previously published assignments.[22] The near-IR absorption spectrum shows many overtones and combination bands that play important roles in the DOVE spectra. For the

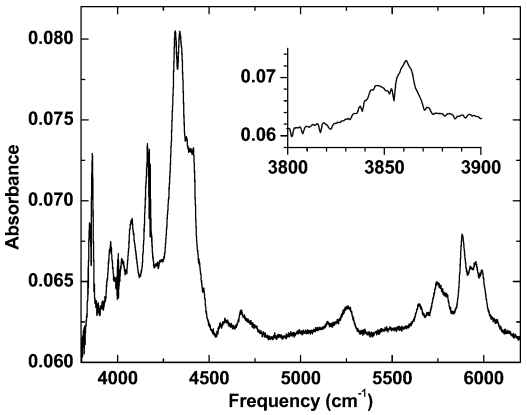

Figure 4. Near-infrared spectrum of crotononitrile.

collection of the IRFWM spectra, the mixture was placed in a thin, flat-faced quartz capillary with an 80-μm sample path length. The absorption from the quartz capillary did not make a significant contribution to the results.

Results

In the first DOVE-FWM experiment, the spectroscopy focused on the expected coupling between the C═C stretching mode, υ_6, and the C≡N stretching mode, υ_5. An expanded view of the υ_5 mode region of the infrared spectrum for the two isomers is shown in Figure 2, whereas an expanded view of the υ_6 mode region of the Raman spectrum is shown in Figure 3. Also visible in Figure 3 are several minor Raman features, including the line from the υ_7 and υ_{18} modes of both isomers at 1443 cm^{-1}; this line is used as an internal Raman standard in the DOVE-FWM experiments. In the absence of anharmonic shifts, Table 1 shows that $\upsilon_5 + \upsilon_6$ combination bands would be expected at 3850.5 (cis) and 3864 cm^{-1}(trans). Figure 4 shows the IR spectrum near this region. There are two peaks visible: one at 3846 cm^{-1} and the other at 3861 cm^{-1} that we assign to the $\upsilon_5 + \upsilon_6$ combination bands.

Figure 5 shows the 2D DOVE-FWM spectrum of crotononitrile. It is a composite of spectra that were taken by scanning ω_1 in step sizes of 0.5 cm^{-1} for different values of ω_2. The spectrum covers the spectral range between $3580 \leq \omega_1 \leq 3920$ cm^{-1} and $2185 \leq \omega_2 \leq 2265$ cm^{-1}. The faint diagonal ridge on the left-hand side of the spectrum is the CARS resonance at $(\omega_1 - \omega_2) = 1443$ cm^{-1} of the υ_7 and υ_{18} modes of the crotononitrile; the peaks for both isomers are at essentially the same position.[22] The υ_7 and υ_{18} modes are degenerate methyl distortion modes, so these modes should not couple well to the C≡N stretching motion; this expectation is supported by the peak position's insensitivity to whether the nitrile is cis or trans to the methyl group. This lack of coupling should prevent any double resonance with the υ_5 mode, so one would expect that its intensity should not depend on the ω_2 value. We therefore use this peak as the internal standard for normalizing each individual spectrum in the composite 2D spectrum. The weakness of the peak compromises a direct normalization of each ω_1 scan in some spectra, so the normalization done for Figure 5 required the simulation procedure described below.

There are two DOVE resonances that dominate the DOVE-FWM spectrum. The left-hand double resonance is the cross peak between υ_5 and $\upsilon_5 + \upsilon_6$ of the cis isomer, whereas the right-hand peak is the corresponding cross peak from the trans isomer. The strong diagonal ridges that pass through the two DOVE resonances are the CARS peaks from the υ_6 modes of the cis (left) and trans (right) isomers of crotononitrile at

TABLE 1: Spectral Parameters Required for Simulations Compared with Values Obtained from Infrared and Raman Spectra[a]

	simulation frequency-Figure 6 (cm^{-1})	simulation frequency-Figure 8 (cm^{-1})	simulation dephasing rate-Figure 6 (cm^{-1})	simulation dephasing rate-Figure 8 (cm^{-1})	IR or Raman frequency (cm^{-1})	IR or Raman line width (cm^{-1})	ϵ (for pure isomers) (L/mol cm)	χ_{Raman} (cm^3/erg)
				cis				
υ_{13} C−CN stretch		889.6		2.8	894	2.6		6.5×10^{-15}
$\upsilon_{7,18}$ CH_3 antisymm. stretch	1445.5		7.6		1443	6.3		
υ_6 C═C stretch	1627.3		4.5		1628.5	3		2.1×10^{-14}
υ_5 C≡N stretch	2225.4	2214	4.0	5.0	2222	3.7	86	
υ_1 HCCH unsymm. stretch		3077		55.0	3077.5			
$\upsilon_5 + \upsilon_{13}$ combination band		3100.1		5.5	3111	4.5	0.152	
$\upsilon_5 + \upsilon_6$ combination band	3845.9		9.0		3846	8	0.62	
$\upsilon_5 + \upsilon_6$, υ_5 coherence	1620.5		3.7					
$\upsilon_5 + \upsilon_{13}$ combination band; υ_5 C≡N stretch coherence		886.1		3.8				
υ_1 HCCH unsymm. stretch; υ_5 C≡N stretch coherence		863		46.0				
				trans				
υ_{13} C−CN stretch		889.6		2.8	894	2.6		6.5×10^{-15}
$\upsilon_{7,18}$ CH_3 antisymm. stretch	1445.5		7.6		1443	6.3		
υ_6 C═C stretch	1637.9		3.0		1638	2		2.5×10^{-14}
υ_5 C≡N stretch	2228.5	2220	4.2	5.0	2226	2.7	92	
υ_1 HCCH unsymm. stretch		3054		52.0	3054			
$\upsilon_5 + \upsilon_{13}$ combination band		3107.2		5.4	3111	4.5	0.152	
$\upsilon_5 + \upsilon_6$ combination band	3859		8.7		3861	5.5	0.92	
$\upsilon_5 + \upsilon_6$, υ_5 coherence	1630.5		3.2					
$\upsilon_5 + \upsilon_{13}$ combination band; υ_5 C≡N stretch coherence		887.2		3.8				
υ_1 HCCH unsymm. stretch; υ_5 C≡N stretch coherence		834		46.0				
C_6D_6 υ_1 ring breathing mode		940.5		1.8				

[a] Assignments are those of Durig.[22]

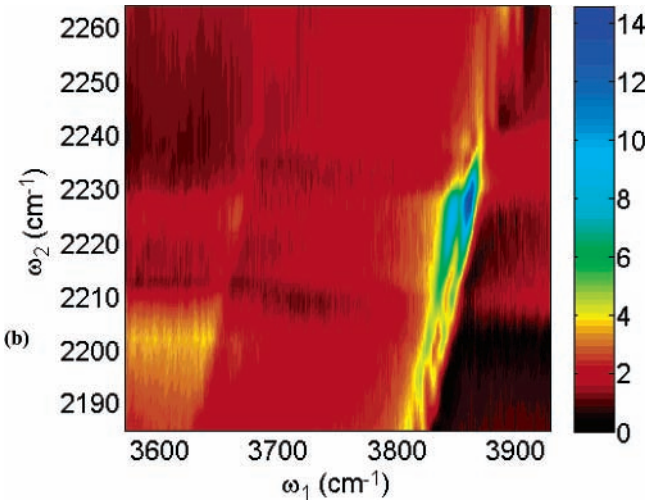

Figure 5. Two-dimensional DOVE-FWM spectrum of crotononitrile in the region of coupling between C═C and C≡N.

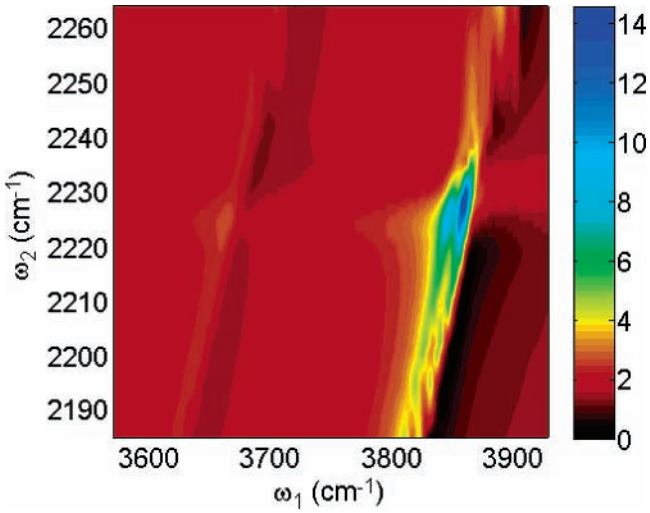

Figure 6. Simulation of two-dimensional DOVE-FWM spectrum of crotononitrile in the region of coupling between C═C and C≡N.

$(\omega_1 - \omega_2) = 1628.5$ and 1638.0 cm^{-1}. The offset of these ridges from the center of the DOVE resonances results from the anharmonicity of the combination band relative to the two fundamentals that create the combination band. The weak trough that extends horizontally to the lower ω_1 frequencies from the DOVE features is the result of the changing absorption from the C≡N mode, as described by the *M* factors in eq 3.

The spectra were simulated using eqs 1−3; the result of this simulation is shown in Figure 6. The simulations include the corrections for the changing sample absorption that are defined by the *M* factors in eq 3. Tables 1 and 2 summarize the values used for the simulations as well as those obtained from infrared and Raman spectra. The values were determined by a least-squares fitting method for the entire set of spectra in Figure 5. The experimental data were first normalized to the peak intensity in each scan of Figure 5, and the simulations were normalized in the same way. Differences in the transition frequencies from the infrared and Raman spectra reflect calibration error. The line widths required for the spectral simulation are generally larger than those observed in the infrared and Raman spectra, although the trends in their differences are similar. The experimental spectra and the simulations were then renormalized by the intensity of the υ_7, υ_{18} CARS contribution in the simulation. Figure 7 shows examples of the fits for representative scans within Figures 5 and 6. The agreement between the data and the simulations is generally good, although the $(\omega_1 - \omega_2) = 1443$ cm^{-1} υ_7/υ_{18} CARS feature is weaker in the experimental data for scans with ω_2 above 2230 cm^{-1}. We

TABLE 2: Summary of Simulation Parameters Used in Fitting Figures 5 and 6

N	7.47×10^{21}
n	1.41
F-crotonitrile	2.41
F-benzene	2.85
D_{DOVE}	6
D_{Raman}	3
$\Delta_{eg}/\Delta_{e}\upsilon$	1.04

component	states	A	B	C
mixture	nonresonant-Figure 6	0.211		
	nonresonant-Figure 8	$0.019e^{0.16\pi i}$		
cis	υ_{13}		0.145	
	υ_7/υ_{18}		1.00	
	υ_6		3.10	
	$\upsilon_5 + \upsilon_6$; υ_6			14.1
	$\upsilon_5 + \upsilon_{13}$, υ_5			−1.8
	υ_1, υ_5			23
trans	υ_{13}		0.145	
	υ_7/υ_{18}		1.00	
	υ_6		2.06	
	$\upsilon_5 + \upsilon_6$; υ_6			28.6
	$\upsilon_5 + \upsilon_{13}$, υ_5			−1.8
	υ_1, υ_5			23.0
C_6D_6	υ_1		2.7	

attribute the suppression to the interference between the CARS feature and the background that is generated by nonlinear processes that are not being considered in the simulation. These processes may also be responsible for the background and the line-shape differences for ω_2 values near 2215 cm^{-1}. It is known that a CARS line can be completely suppressed if the magnitude of the background is half of the peak CARS value and if the background is imaginary.[13]

One can obtain the real and imaginary parts of the third-order nonlinearities of each of the nonlinear processes in our experiments from the simulations by comparing the spectra with a standard whose third-order nonlinearity is known. Previous work by Levenson and Bloembergen established that $\chi^{(3)}$ for the Raman transition of the 992-cm^{-1} ring-breathing mode of benzene is 1.6×10^{-13} cm^3/erg in the Maker-Terhune convention.[18,19,23] Because this determination used two-laser coherent anti-Stokes Raman spectroscopy (CARS) with visible lasers, the value must be corrected to the conditions of this experiment where two of the frequencies are infrared and one is visible and three separate laser frequencies are used. Using the previously published method for correcting the values, we obtain a value of 7.1×10^{-14} cm^3/erg for benzene's Raman susceptibility, or $\gamma = 3.7 \times 10^{-36}$ cm^6/erg for the hyperpolarizability.[4] Because the internal standard for this work is the $(\omega_1 - \omega_2) = 1443$ cm^{-1} Raman transition of crotononitrile, it is necessary to determine its corresponding $\chi^{(3)}$ relative to that of benzene. A Raman spectrum of a 4:1 mol/mol mixture of crotononitrile (~1:1 cis/trans, as above) and benzene was used to determine the relative size of the two Raman hyperpolarizabilities. This procedure gave a value of $\gamma = 9.9 \times 10^{-38}$ cm^6/erg for the $(\omega_1 - \omega_2) = 1443$ cm^{-1} mode of crotononitrile. Because both isomers contribute to this peak, this γ represents a composite value for the sum of the two isomers at the abundances at which they are present in the mixture. The Raman spectrum also provided values of $\gamma = 1.6 \times 10^{-37}$ and 1.9×10^{-37} cm^6/erg for the υ_6 modes of the cis and trans isomers, respectively. Again, these values correspond to three-laser CARS using two infrared excitations.

The hyperpolarizabilities are now determined using eq 1. The peak hyperpolarizabilities are A, $(iB/\Gamma_{\upsilon g})$, $(C/\Gamma_{\upsilon'' g}\Gamma_{\upsilon'' \upsilon'})$, $(C/\Gamma_{\upsilon' g}\Gamma_{\upsilon'' \upsilon'})$, and $-(C/\Gamma_{\upsilon'' g}\Gamma_{\upsilon g})$ for the nonresonant, CARS, DOVE-IRα, DOVE-IRβ, and DOVE-Raman pathways, respectively. The values in Tables 1 and 2 were used to find the peak hyperpolarizabilities, and these are summarized in Table 3 along

TABLE 3: Summary of the Experimental Hyperpolarizabilities and Third-Order Susceptibilities for Each of the Processes That Are Important for the DOVE-FWM Spectra Simulated in Figure 8[a]

nonlinear process	modes	γ exptl	$\chi^{(3)}$ exptl	γ calcd	$\chi^{(3)}$ calcd
		cis			
DOVE-IRα	$\upsilon_5 + \upsilon_6$; υ_5	1.59×10^{-37}	2.88×10^{-15}	4.0×10^{-37}	7.2×10^{-15}
DOVE-IRβ	$\upsilon_5 + \upsilon_6$; υ_5	3.59×10^{-37}	6.47×10^{-15}	8.9×10^{-37}	1.6×10^{-14}
DOVE-Raman	$\upsilon_5 + \upsilon_6$; υ_5	-1.31×10^{-37}	-2.36×10^{-15}	-3.3×10^{-37}	-5.9×10^{-15}
DOVE-IRα	$\upsilon_5 + \upsilon_{13}$, υ_5	-2.13×10^{-37}	-3.84×10^{-15}	-9.1×10^{-38}	-1.6×10^{-15}
DOVE-IRβ	$\upsilon_5 + \upsilon_{13}$, υ_5	-2.34×10^{-37}	-4.22×10^{-15}	-1.0×10^{-37}	-1.8×10^{-15}
DOVE-Raman	$\upsilon_5 + \upsilon_{13}$, υ_5	2.89×10^{-37}	5.2×10^{-15}	1.8×10^{-37}	3.2×10^{-15}
DOVE-IRα	υ_1, υ_5	1.61×10^{-38}	2.91×10^{-16}	7.8×10^{-40}	1.4×10^{-17}
DOVE-IRβ	υ_1, υ_5	1.78×10^{-37}	3.20×10^{-15}	1.4×10^{-39}	2.5×10^{-17}
DOVE-Raman	υ_1, υ_5				
CARS	υ_{13}	1.28×10^{-37}	2.31×10^{-15}		
CARS	υ_7/υ_{18}	9.91×10^{-38}	1.79×10^{-15}		
CARS	υ_6	2.59×10^{-37}	4.68×10^{-15}		
		trans			
DOVE-IRα	$\upsilon_5 + \upsilon_6$; υ_5	3.87×10^{-37}	6.98×10^{-15}	5.3×10^{-37}	9.6×10^{-15}
DOVE-IRβ	$\upsilon_5 + \upsilon_6$; υ_5	8.02×10^{-37}	1.45×10^{-14}	1.1×10^{-36}	2.0×10^{-14}
DOVE-Raman	$\upsilon_5 + \upsilon_6$; υ_5	-4.13×10^{-37}	-7.45×10^{-15}	-5.7×10^{-37}	-1.0×10^{-14}
DOVE-IRα	$\upsilon_5 + \upsilon_{13}$, υ_5	-2.17×10^{-37}	-3.91×10^{-15}	-9.2×10^{-38}	-1.7×10^{-15}
DOVE-IRβ	$\upsilon_5 + \upsilon_{13}$, υ_5	-2.34×10^{-37}	-4.22×10^{-15}	-9.9×10^{-38}	-1.78×10^{-15}
DOVE-Raman	$\upsilon_5 + \upsilon_{13}$, υ_5	2.94×10^{-37}	5.30×10^{-15}	1.8×10^{-37}	3.24×10^{-15}
DOVE-IRα	υ_1, υ_5	2.38×10^{-38}	4.28×10^{-16}	8.9×10^{-40}	1.60×10^{-17}
DOVE-IRβ	υ_1, υ_5	2.47×10^{-37}	4.4×10^{-15}	1.6×10^{-39}	2.80×10^{-17}
DOVE-Raman	υ_1, υ_5				
CARS	υ_{13}	1.28×10^{-37}	2.31×10^{-15}		
CARS	υ_7/υ_{18}	9.91×10^{-38}	1.79×10^{-15}		
CARS	υ_6	2.59×10^{-37}	4.66×10^{-15}		
nonresonant	Figure 6 simulation	8.0×10^{-38}	1.43×10^{-15}		
nonresonant	Figure 8 simulation	4.7×10^{-38}	8.47×10^{-16}		

[a] A comparison is shown with the values calculated from the infrared and Raman spectra.

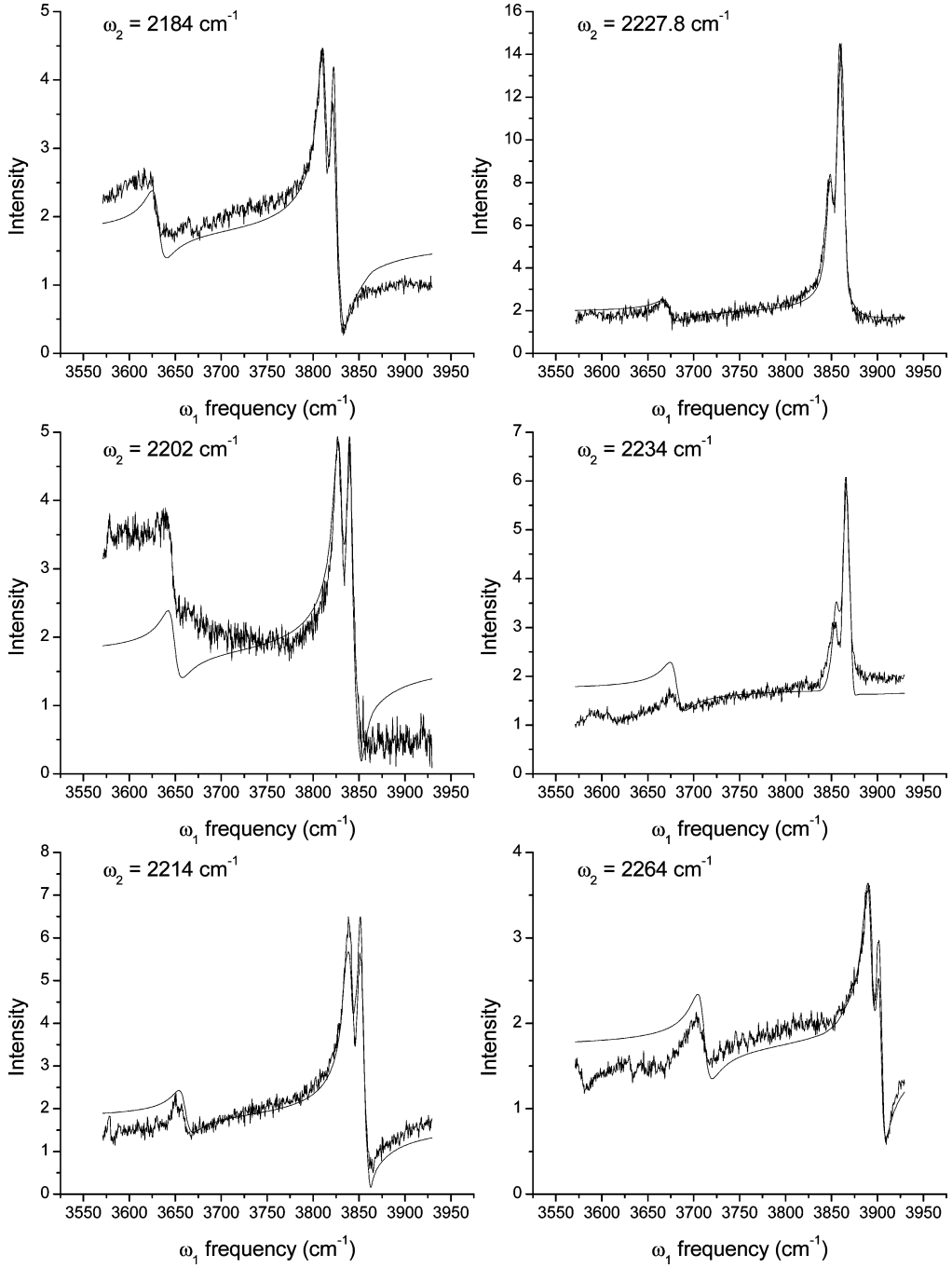

Figure 7. One-dimensional slices through the DOVE spectra in Figures 5 and 6.

with the third-order nonlinear susceptibilities, $\chi^{(3)}$, obtained using eq 2. The $\chi^{(3)}$ values calculated using eq 2 assumed a pure isomeric sample. The nonlinearity for the DOVE-IRβ pathway is significantly larger than that for the other pathways. The DOVE-IRα and DOVE-Raman pathways have smaller nonlinearities because they involve a large $\Gamma_{v''g}$ dephasing rate.

All of the DOVE processes involve three transitions: two infrared absorption/emission transitions and one Raman transition. The transition dipoles involved in each transition are related directly to the corresponding spectral features in the infrared absorption and Raman spectra. It is possible to estimate the third-order susceptibilities from the linear infrared absorption coefficient and the Raman $\chi^{(3)}_{i,j,k,l}$

$$\alpha = \frac{4\pi\omega NF\mu^2\rho_{gg}}{n\hbar c\Gamma} \tag{4}$$

$$\chi^{(3)}_{vg,\mathrm{Raman}} = \frac{\mathrm{i}NF_3{}^2F_4\mu^i_{ge}\mu^j_{ev}\mu^k_{ve}\mu^l_{eg}\rho_{gg}}{4D_{\mathrm{Raman}}\hbar^3(\omega_{eg}-\omega_3-\mathrm{i}\Gamma_{eg})(\omega_{eg}-\omega_4-\mathrm{i}\Gamma_{eg})\Gamma_{vg}} \tag{5}$$

where e labels the nonresonant electronic state and c is the speed of light; we approximate the Raman susceptibility by considering only the dominant pathway and a single "effective" electronic state.[24] D_{Raman} is a degeneracy factor that depends on the convention for defining $\chi^{(3)}$.[23] In the Maker-Terhune convention, it is 3 for a two-laser experiment and 6 for a three-laser experiment.[23] The Raman process involves frequencies ω_3 and ω_4 in a DOVE experiment. Equation 5 is related to a CARS process involving the same vibrational state. For the three-laser CARS processes in this work,

$$\chi^{(3)}_{\nu g,\mathrm{CARS}} = \frac{\mathrm{i}NF_1F_2F_3\mu^i_{ge}\mu^j_{e\nu}\mu^k_{\nu e}\mu^l_{eg}\rho_{gg}}{4D_{\mathrm{CARS}}\hbar^3(\omega_{eg}-\omega_1-\mathrm{i}\Gamma_{eg})(\omega_{eg}-\omega_4-\mathrm{i}\Gamma_{eg})\Gamma_{\nu g}} \quad (6)$$

It is important to remember that eq 5 expresses the $\chi^{(3)}$ for a normal Raman transition involving two interactions with one field and one interaction with the second field to produce an output at the second field's frequency and a vibrational excitation. The $\chi^{(3)}$ values tabulated in Table 3 and defined by eq 6 correspond to a CARS process involving the same vibrational state, but it requires interactions with two different infrared fields and one interaction with a visible field to produce an output at the anti-Stokes frequency. Using the 1.6×10^{-13} cm^3/erg value of $\chi^{(3)}$ from the Levenson and Bloembergen two-color CARS experiment[18,19,23] and the ratios of the hyperpolarizabilities determined for the cis and trans υ_6 modes (above), the values for $\chi^{(3)}_{\nu g,\mathrm{Raman}}$ are 2.1×10^{-14} and 2.5×10^{-14} cm^3/erg, respectively. By solving for the transition moments in eqs 4 and 5, suppressing the tensorial nature of $\chi^{(3)}$, and substituting into the peak DOVE-IR $\chi^{(3)}$, one finds

$$\chi^{(3)}_{\mathrm{DOVE-IR}\alpha} = \frac{c\Delta_{eg}}{8\pi D_{\mathrm{DOVE}}\Delta_{e\nu}\Gamma_{\nu''\nu'}}\sqrt{\frac{F_3D_{\mathrm{Raman}}\alpha_{\nu''g}\alpha_{\nu'g}\chi_{\mathrm{Raman}}\Gamma_{\nu'g}\Gamma_{\nu g}}{\hbar\omega_1\omega_2\Gamma_{\nu''g}N\rho_{gg}}} \quad (7)$$

$$\chi^{(3)}_{\mathrm{DOVE-IR}\beta} = \frac{\Gamma_{\nu''g}}{\Gamma_{\nu'g}}\chi^{(3)}_{\mathrm{DOVE-IR}\alpha} \quad (8)$$

$$\chi^{(3)}_{\mathrm{DOVE-Raman}} = \frac{\Gamma_{\nu''\nu'}}{\Gamma_{\nu g}}\chi^{(3)}_{\mathrm{DOVE-IR}\alpha} \quad (9)$$

Table 3 summarizes the calculated values of the nonlinearities using the transition frequencies, dephasing rates, and absorption coefficients determined by the simulations and eqs 7−9. Note that the detuning factors, Δ_{eg} and $\Delta_{e\nu}$, in eq 7 appear as a ratio that is quite close to unity because the effective excited electronic state is much larger than a vibrational frequency and the ratio is insensitive to the exact value of the effective state energy. The experimental values obtained by the simulations are in reasonable agreement with the values calculated from eqs 7−9.

We also studied the mode coupling between the crotononitrile υ_5 C≡N and υ_{13} C−CN stretching modes. One would expect the coupling to be similar to that seen in acetonitrile because the modes are quite similar. The inset of Figure 3 shows the region of the υ_{13} C−CN stretching modes. There is a single peak at the position of this mode, so the frequencies of the two isomers are the same within the transition line width. The inset of Figure 2 shows the region of the infrared spectrum for the $\upsilon_5 + \upsilon_{13}$ combination bands that would be associated with the coupling between the two modes. In the absence of an anharmonic shift, these combination bands are expected at 3116 (cis) and 3120 cm^{-1} (trans). In the spectrum, a peak is visible at 3111 cm^{-1}, with a weaker companion at 3122 cm^{-1}. Although it might be tempting to assign the lower-energy peak to the cis combination band and the higher-energy peak to the trans combination band, this assignment would involve anharmonic shifts in opposite directions. Instead, we assign the peak at 3111 cm^{-1} to both combination bands, with its large line width (~4.5 cm^{-1}), low intensity, and interference from the large tail of the cis υ_1 obscuring the splitting.

The DOVE-FWM spectra for a 35:3 mole ratio of crotononitrile and deuteriobenzene are shown in Figure 8 for ω_1 values from 3030 to 3250 cm^{-1} and ω_2 values from 2190 to 2240 cm^{-1}. Because the scans are done separately from those in Figure 5, experimental error makes the frequency calibration different. The frequencies obtained by a least-squares simulation are summarized in Table 1. The Tables include an extra significant figure in the frequencies because the simulation results are quite sensitive to the relative frequency differences. Deuteriobenzene was added as an internal standard. These spectra were acquired at a phase-matching angle of 14.2°, and each spectrum was normalized to the height of the deuteriobenzene ring-breathing mode CARS line at $(\omega_1 - \omega_2) = 944$ cm^{-1}. The absolute signal strength is weak in the region of the C≡N mode because the strong absorption of the ω_2 beam decreases the effective-mixing path length.

The strongest peak on the right-hand side of Figure 8 is the deuteriobenzene CARS feature, whereas the weaker and more diffuse features on the left-hand side of the spectrum result from interference between the *cis*- and *trans*-crotonitrile CARS pathway involving the υ_{13} C−C stretching mode and the DOVE-IR and DOVE-Raman pathways involving the υ_5 and υ_{13} modes and the $(\upsilon_5 + \upsilon_{13})$ combination band. As ω_2 is changed across the C≡N stretching frequency, the features in Figure 8 shift such that $(\omega_1 - \omega_2) = 890$ cm^{-1}. The CARS component of this feature always occurs at $(\omega_1 - \omega_2) = 890$ cm^{-1} and must be the dominant component when the fixed value of ω_2 does not allow double resonances. Because the feature has the same positively dispersive line shape as the deuteriobenzene feature (i.e., it has a peak on the high-frequency side and a trough on the low-frequency side) at low and high values of ω_2, the sign of B in the CARS term of eq 1 is the same for both features and must be positive. The $(\omega_1 - \omega_2) = 890$ cm^{-1} feature becomes negatively dispersive as ω_2 nears the C≡N resonance and the DOVE processes become important. The peak is hidden in the background at low ω_2 frequencies because the CARS resonance is obscured by destructive interference between the CARS and the DOVE-Raman process. The CARS process is described by $B/(\omega_{ag} - \omega_1 + \omega_2 - \mathrm{i}\Gamma_{ag})$, whereas the DOVE-Raman process is described by $C/\{(\omega_{cg} - \omega_1 - \mathrm{i}\Gamma_{cg})(\omega_{ag} - \omega_1 + \omega_2 - \mathrm{i}\Gamma_{ag})\}$. The two processes share a common resonance, but the DOVE-Raman process has an extra resonance factor that can be positive for $\omega_1 \ll \omega_{cg}$, imaginary for $\omega_1 = \omega_{cg}$, and negative for $\omega_1 \gg \omega_{cg}$. The resulting interference can eliminate or enhance the CARS resonance, depending upon the relative sign and magnitude of B and C. The data show that the CARS resonance disappears for the low ω_2 frequencies, so the two processes destructively interfere in this region and the amplitude for the DOVE processes must have the opposite sign to that of the CARS process.

As ω_2 nears the C≡N resonances, the DOVE-Raman process is enhanced until it dominates in importance over the CARS process. The line shape has the opposite dispersive character because of the difference in sign between the CARS and the DOVE-Raman process. The DOVE-Raman process is maximally enhanced when $\omega_1 = \omega_{cg}$ and $\omega_2 = \omega_{cg} - \omega_{ag}$. As ω_2 moves across the crotononitrile ν_5 resonances, the features' line shape continues to change because of the differences in the relative contributions from the DOVE-IR, DOVE-Raman, and CARS pathways. The DOVE-IR pathways are maximally enhanced when $\omega_1 = \omega_{cg}$ and when $\omega_2 = \omega_{bg}$. At ω_2 frequencies that are much higher than the υ_5 resonances, the features become a normal, positively dispersive CARS line for υ_{13} as the DOVE processes become less important and the CARS process

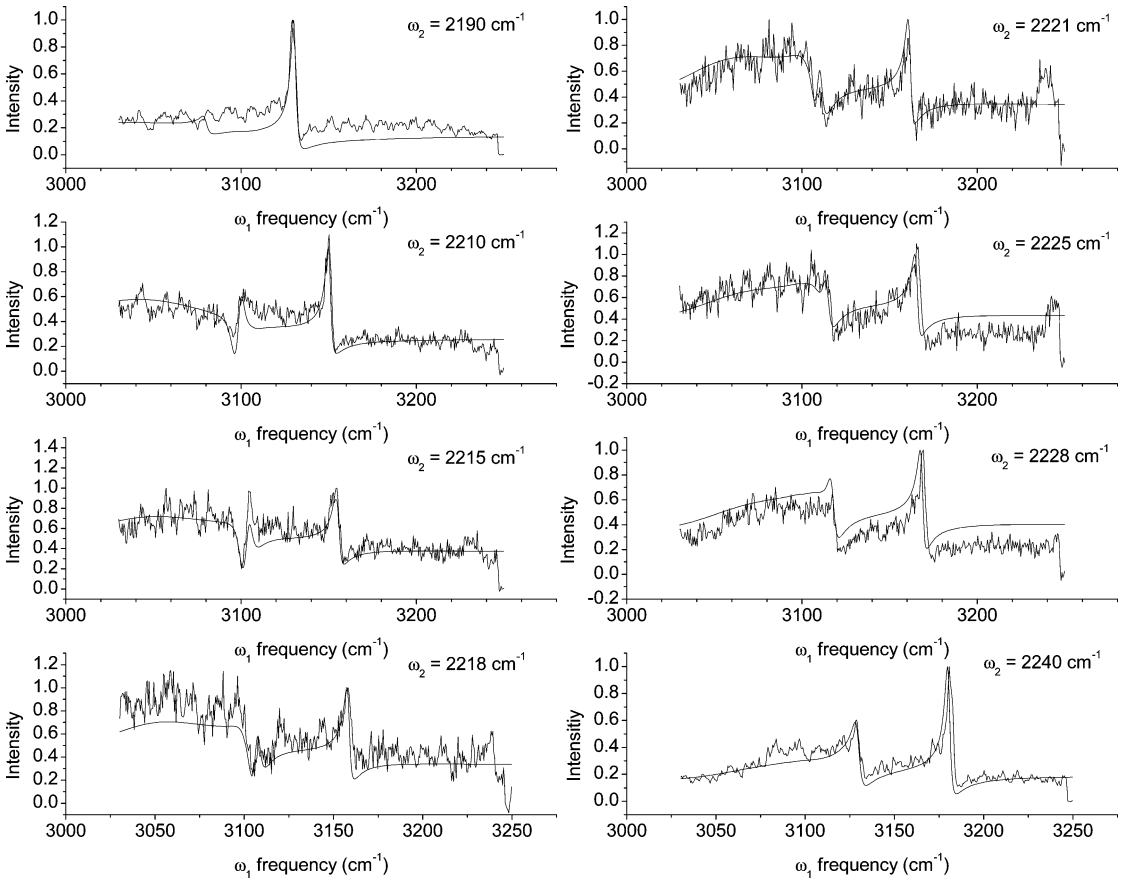

Figure 8. Experimental results and simulations of DOVE spectra of crotononitrile in the region of the coupling between the C−C and C≡N stretching modes.

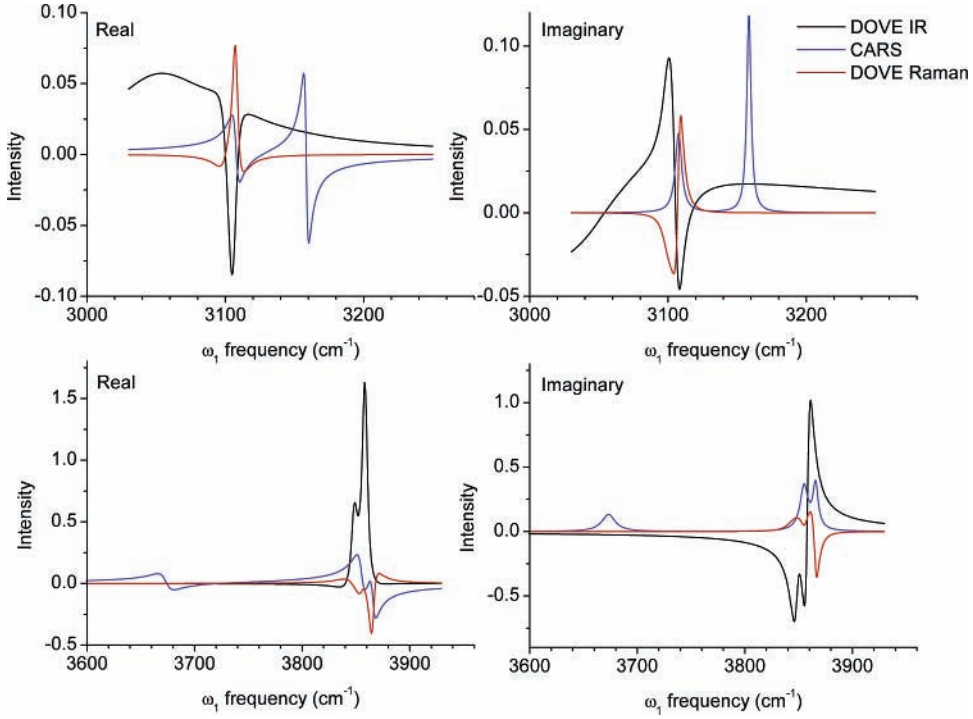

Figure 9. Real and imaginary parts of $\chi(3)$ for the DOVE-IR, DOVE-Raman, and CARS processes when ω_2 is resonant with the cis C≡N stretching mode. Note the destructive interference between the different nonlinear processes in the top row that reduces the intensity of the DOVE peak.

dominates. This behavior is the signature of the interference between the CARS line and the DOVE resonances.[4]

To extract quantitative values for the DOVE nonlinearities, we simulated the spectra by a least-squares fitting to eqs 1−3, and the values listed in Tables 1 and 2. The simulations include the corrections for the changing sample absorption that are defined by the *M* factors in eq 3. The values required for the simulations are consistent with those expected on the basis of infrared and Raman data and previous experiments;[22] the simulation results are shown in Figure 8 for comparison to the

data. The fitting is improved considerably by including a DOVE-IR process involving the υ_1 HCCH unsymmetrical stretch and the υ_5 C≡N stretch fundamentals, although there is no signature in the spectra that gives confidence that this process is important. The evidence for a DOVE process involving the υ_1 and υ_5 modes is largely from the elevation and shape of the baseline in the spectra when ω_2 is resonant with the C≡N stretching mode. Also note that the Γ value required for fitting this process is larger than that observed for the infrared spectrum of this mode. The large Γ may simply represent an effective dephasing rate that actually represents a DOVE and SIVE (singly vibrationally enhanced) FWM process involving the other C−H stretching modes or underlying combination bands, but it could also indicate that the process is not important.

It is interesting to compare the DOVE spectra involving the C−C and the C═C stretching regions. All of the $\chi^{(3)}$ values for crotonitrile are appreciably smaller than those seen in acetonitrile.[13] The biggest difference is in the sign of the DOVE contribution. The sign of the *C* amplitude involving the υ_{13} C−C stretch is the same as that observed previously in acetonitrile and deuterioacetonitrile, whereas it has the opposite sign when the υ_6 C═C stretch is involved.[13] It was shown earlier that the overall sign of the DOVE processes depends on a variety of anharmonic and nonlinear couplings involving all of the molecular modes.[25] The net sign depends on the relative magnitudes and signs of many processes and can be either positive or negative. The sign has an interesting effect on the character of the spectrum because it controls how the DOVE pathways interfere with the CARS pathway.

The spectral features involving the C−C mode in Figure 8 are weaker and have a different character than those involving the C═C mode in Figures 5 and 6. The latter features are much more sharply defined. The difference arises from the interference effects and relative sizes of the three DOVE pathways. The peak values of $\chi^{(3)}$ are given by $(C/\Gamma_{\upsilon''g}\Gamma_{\upsilon''\upsilon'})$, $(C/\Gamma_{\upsilon'g}\Gamma_{\upsilon''\upsilon'})$, and $-(C/\Gamma_{\upsilon''g}\Gamma_{\upsilon g})$ for the two DOVE-IR pathways and the DOVE-Raman pathway, respectively. Figure 9 compares the real and imaginary values of the simulated $\chi^{(3)}$ when ω_2 is resonant with the C≡N stretching mode for each pathway. The contributions from each pathway add to create the net polarization. Although the DOVE-IRβ pathway is particularly strong for the DOVE processes involving the C═C stretching mode (Table 3), there is also constructive interference between the pathways that augments the size of the doubly resonant peak. The values of $\chi^{(3)}$ are smaller for the DOVE processes involving the C−C stretching mode, and the pathways shown in Figure 9 have contributions that cancel. Both of these effects lead to the weakness of the observed DOVE features in Figure 8.

Conclusions

Two-dimensional DOVE experiments have been performed on crotononitrile, and two regions have been identified that show the coupling between the C≡N stretch and the C═C and C−C stretching modes. The results have provided a comparison to the earlier DOVE experiments in acetonitrile, and we find that the coupling is smaller for both regions.[13] The 2D spectrum also resolves the vibrational features of the cis and trans isomers in the C═C and C≡N stretch combination band ($\upsilon_5 + \upsilon_6$) cross peak. The spectra can be quantitatively understood by including an internal standard in the experiment and simulating the 2D spectra. In infrared absorption and Raman spectroscopy, the dephasing rates are determined by the line width of the homogeneous or Lorentzian part of the line shape. In the DOVE experiments, the dependence of the 2D spectra on dephasing rates is more complex. The line shapes are not Lorentzians, even if the line broadening is homogeneous. The line shapes are defined by the amplitude-level interference between the two important DOVE-IR and the single DOVE-Raman pathways. Because the relative contribution from each pathway depends on the coherences' dephasing rate, both the line shape and the line intensity depend on the dephasing rates. If there is a inhomogeneous broadening component that is correlated between the different vibrational modes, then the effects appear as narrowing, and shifts in line position as well as changes in line width occur. There are therefore multiple spectral signatures of both homogeneous and inhomogeneous broadening effects that make coherent multidimensional spectroscopy sensitive to the size of the nonlinearities, the dephasing rates, and the inhomogeneous broadening. By fitting the experimental data with simulations of the spectra, we have shown that one can determine all of the nonlinearities and dephasing times quantitatively. We did not see any evidence for inhomogeneous broadening effects in the spectra.

Acknowledgment. This work was supported by the Chemistry Program of the National Science Foundation under grant CHE-0130947.

References and Notes

(1) Wright, J. C. *Int. Rev. Phys. Chem.* **2002**, *21*, 185.
(2) Mukamel, S. *Annu. Rev. Phys. Chem.* **2000**, *51*, 691.
(3) Meyer, K. A.; Wright, J. C. *Chem. Phys. Lett.* **2003**, *381*, 642.
(4) Zhao, W.; Wright, J. C. *Phys. Rev. Lett.* **1999**, *83*, 1950.
(5) Zhao, W.; Wright, J. C. *J. Am. Chem. Soc.* **1999**, *121*, 10 994.
(6) Zhao, W.; Wright, J. C. *Phys. Rev. Lett.* **2000**, *84*, 1411.
(7) Asplund, M. C.; Zanni, M. T.; Hochstrasser, R. M. *Proc. Natl. Acad. Sci. U.S.A.* **2000**, *97*, 8219.
(8) Zanni, M. T.; Asplund, M. C.; Hochstrasser, R. M. *J. Chem. Phys.* **2001**, *114*, 4579.
(9) Zanni, M. T.; Gnanakaran, S.; Stenger, J.; Hochstrasser, R. M. *J. Phys. Chem. B* **2001**, *105*, 6520.
(10) Hamm, P.; Lim, M.; Hochstrasser, R. M. *J. Phys. Chem. B* **1998**, *102*, 6123.
(11) Hamm, P.; Lim, M.; DeGrado, W. F.; Hochstrasser, R. M. *Proc. Natl. Acad. Sci. U.S.A.* **1999**, *96*, 2036.
(12) Hamm, P.; Lim, M.; DeGrado, W. F.; Hochstrasser, R. M. *J. Chem. Phys.* **2000**, *112*, 1907.
(13) Wright, J. C.; Condon, N. J.; Murdoch, K. M.; Besemann, D. M.; Meyer, K. A. *J. Phys. Chem. A* **2003**, *107*, 8166
(14) Lee, D.; Albrecht, A. C. *Advances in Infrared and Raman Spectroscopy*, 1st ed.; Wiley-Heyden: Chichester, England, 1985; Vol. 12.
(15) Carlson, R. J.; Wright, J. C. *Appl. Spectrosc.* **1989**, *43*, 1195.
(16) Murdoch, K. M.; Thompson, D. E.; Meyer, K. A.; Wright, J. C. *Appl. Spectrosc.* **2000**, *54*, 1495.
(17) Thompson, D. E.; Wright, J. C. *J. Phys. Chem. A* **2000**, *104*, 11 282.
(18) Levenson, M. D.; Bloembergen, N. *Phys. Rev. B* **1974**, *10*, 4447.
(19) Levenson, M. D.; Bloembergen, N. *J. Chem. Phys.* **1974**, *60*, 1323.
(20) Chen, P. C.; Hamilton, J. P.; Zilian, A.; LaBuda, M. J.; Wright, J. C. *Appl. Spectrosc.* **1998**, *52*, 380.
(21) Zhao, W.; Murdoch, K. M.; Besemann, D. M.; Condon, N. J.; Meyer, K. A.; Wright, J. C. *Appl. Spectrosc.* **2000**, *54*, 1000.
(22) Durig, J. R.; Tong, C. K.; Hawley, C. W.; Bragin, J. *J. Phys. Chem.* **1971**, *75*, 44.
(23) Levenson, M. D.; Kano, S. S. *Introduction to Nonlinear Spectroscopy*; Academic Press: New York, 1988.
(24) Besemann, D.; Condon, N.; Meyer, K.; Zhao, W.; Wright, J. C. *Bull. Korean Chem. Soc.* **2003**, *24*, 1119.
(25) Kwak, K.; Cha, S.; Cho, M. H.; Wright, J. C. *J. Chem. Phys.* **2002**, *117*, 5675.